Short thesis for the degree of doctor of philosophy (PhD)

Nanoscale structural characteristics of polyvinyl alcohol – borosilicate hybrid aerogels and calcium alginate aerogels for potential biomedical applications

by **Zoltán Balogh**

Supervisors:
Dr. József Kalmár, Associate Professor
Dr. Zoltán Imre Dudás, Senior Research Fellow

UNIVERSITY OF DEBRECEN
Doctoral School of Chemistry

Debrecen, 2024.

Abbreviations

BSP	Borosilicate – polyvinyl alcohol hybrid gel
DPSC	Dental Pulp Stem Cell
EDS	Energy Dispersive X-ray Spectroscopy
FT-IR	Fourier-Transform Infrared spectroscopy
HAp	Hydroxyapatite
ICP-OES	Inductively Coupled Plasma – Optical Emission Spectrometry
PVA	Polyvinyl alcohol
SANS	Small-Angle Neutron Scattering
SEM	Scanning Electron Microscopy
SLD	Scattering-length density
ssNMR	Solid-state Nuclear Magnetic Resonance
TEM	Transmission Electron Microscopy
V/V%	Volume percent
w/w%	Weight percent
XRD	X-ray Diffraction

I. Introduction and research objectives

Aerogels are such solid gels where the solvent is replaced by air without significantly altering their original backbone, which is typically realized by supercritical drying. They have open and interconnected mesoporous structures with high specific surface areas (400-1200 m^2/g) and low envelope densities (0.02-0.50 g/cm^3).

The synthesis of the gel backbone is generally achieved by the sol-gel method from a reactant solution and results in a two-phase system, namely the solid backbone and the pore-filling solvent. There are several possibilities to form a gel from different types of precursors. The literature provides examples of aerogels made from inorganic, organic, or (bio)polymer precursors, or even from different types of precursors simultaneously in the form of hybrids.

Aerogels can be utilized in many fields of industry due to their chemical and structural diversity provided by the versatile synthesis routes. Along with the appearance of (bio)polymer and hybrid aerogels, much research has been started recently on their biomedical applications, such as drug delivery and tissue engineering.

Designing chemical and morphological features with the intention to benefit a chosen application is not trivial. However, exploring the structural properties of advanced materials that show promising results in the selected field of application can provide information on the crucial factors that enable high performance.

Two studies are presented that focus on the detailed investigation of the structures of aerogels and the structural changes that occur during their use. In the first study, we investigated the nanostructure of newly synthesized borosilicate – polyvinyl alcohol (PVA) hybrid aerogels with potential use in bone regeneration. We took special care to investigate the morphological changes that occur when the hybrid aerogels interact with water.

In the other study, the focus is on the development of a mathematical model that sufficiently describes the hydration-induced morphological changes of a typical calcium alginate aerogel based on small-angle neutron scattering (SANS) measurements. The investigation of this phenomenon is crucial, because the focus of the application of this aerogel is in the fields of drug delivery and wound healing, where interactions with water are inevitable.

II. Methods

The synthesis of new Ca(II)-doped borosilicate – PVA (BSPXY) aerogels was performed using the sol-gel method. The gels were dried in an autoclave reactor in supercritical CO_2. The BSPXY code system is used to differentiate the as-prepared aerogels based on their compositions. The BSP refers to the borosilicate-PVA hybrid gel, X refers to the molecular weight of the PVA (X = 13/49/89 if the molecular weight of the PVA is 13/49/89 kDa), and Y refers to the Ca(II) source (no Ca(II) source = 0; $CaCl_2$ = Cl; β-$Ca_3(PO_4)_2$ = P; hydroxyapatite = H).

Various characterization techniques were employed to obtain a comprehensive understanding of the structure of the newly synthesized BSPXY hybrid aerogels, as well as the structural changes that occur when the molecular weight of the PVA and/or the incorporated Ca(II) source are altered. The chemical composition of the aerogels was investigated using Fourier-transform infrared spectroscopy (Perkin Elmer Spectrum Two FT-IR Spectrometer) and solid-state Nuclear Magnetic Resonance spectroscopy (600 MHz Varian Spectrometer equipped with a 3.2 mm HX magic-angle spinning (MAS) probe). The ssNMR measurements were performed by Dr. Andraž Krajnc of the Slovenian National Institute of Chemistry.

The morphology of the aerogels was investigated using scanning (Thermo Fisher Scientific Scios 2) and transmission electron microscopy techniques (CS corrected Thermo Fisher Themis TEM) along with N_2 adsorption-desorption porosimetry (Quantachrome Nova 2000e). SEM images provide visual information on the 3D structure of the gel backbone at the nanometer scale, while TEM images offer insights into the substructure of the nanoparticles forming the backbone. N_2 adsorption-desorption porosimetry provides information on the pore size distribution in the mesopore range, as well as the pore volume and specific surface area of the aerogels.

To determine the amount of incorporated Ca(II) sources, the aerogel backbones were first digested in a harsh chemical environment, and the Ca(II) content was then measured by inductively coupled plasma optical emission spectrometry (ICP-OES, using an Agilent 5100 SVDV spectrometer). Energy-dispersive X-ray spectroscopy (EDS) elemental maps were also recorded using the TEM instrument in scanning mode to analyze the size and location of the incorporated calcium sources. X-ray diffraction (Rigaku SmartLab 9.0 kW X-ray diffractometer) measurements were performed on both the raw Ca(II) sources and the incorporated ones to gain information on their crystalline structure.

Small-angle neutron scattering (Yellow Submarine pinhole-type SANS instrument at the Budapest Neutron Centre) measurements were performed on dry and wet BSPXY aerogel samples to study their nanoscale characteristics. The scattering curves of the dry samples provide information on the fractal nature and the size of scattering objects in the nanometer range, such as pores and particle agglomerations. Wet samples were also studied to observe potential morphological changes of the aerogels in aqueous conditions. Contrast variation measurements were also performed, by filling the aerogels with a mixture of H_2O and D_2O in different ratios. These measurements provide insights into the hybrid nature of Ca(II)-free samples, and for Ca(II)-containing samples, additional information on the Ca(II) source.

The ζ-potential of the suspended aerogel particles was measured in the pH range of 3 to 8 using a MALVERN Zetasizer Nano ZS instrument. The ζ-potential provides information on the electrostatic double layer surrounding the suspended particles. This colloidal property is important as it influences the interactions between the suspended aerogel particles and cells.

The development of a material-specific SANS model to describe hydration-induced morphological changes in a typical calcium alginate aerogel was realized in collaboration with Dr. Cédric J. Gommes, associate professor at the University of Liège. The scattering curves were previously published in an article[1], where a qualitative model for these changes was proposed. Our goal was to develop a new mathematical approach for these scattering curves to get quantitative information on the morphological changes. The morphological and chemical properties of the dry calcium alginate aerogel, as well as the gyration radius and the polymer volume of the hydrated alginate polymer chain was considered for setting up the model. The model was tested in MATLAB software and the data fitting was performed using a non-linear least-squares algorithm.

---

[1] Forgács, A.; Papp, V.; Paul, G.; Marchese, L.; Len, A.; Dudás, Z.; Fábián, I.; Gurikov, P.; Kalmár, J., Mechanism of Hydration and Hydration Induced Structural Changes of Calcium Alginate Aerogel. *ACS Applied Materials & Interfaces* **2021,** *13* (2), 2997-3010. **10.1021/acsami.0c17012**

III. New scientific results

1. Synthesis of new borosilicate – polyvinyl alcohol hybrid aerogels.

1.1.) The synthesis of borosilicate–PVA hybrid gels was performed using a sol-gel method. First, acidic conditions were applied to promote the hydrolysis of the silica precursor. In the second step, boric acid and PVA solutions were added to form a hybrid gel, followed by the addition of NH_4F catalyst to initiate gelation. Three different molecular weight PVAs (13–23 kDa, 49 kDa, and 89–98 kDa) were used. The resulting gels were solvent-exchanged in multiple steps, then dried under supercritical conditions.

1.2.) To prepare Ca(II) containing gels, three different types of Ca(II) sources were used, namely $CaCl_2$, β-$Ca_3(PO_4)_2$ and hydroxyapatite ($Ca_{10}(PO_4)_6(OH)_2$ – HAp). The Ca(II) sources were added to the reaction mixture right after the boric acid and PVA solutions. The rest of the synthesis route remained unchanged (**Fig. 1**).

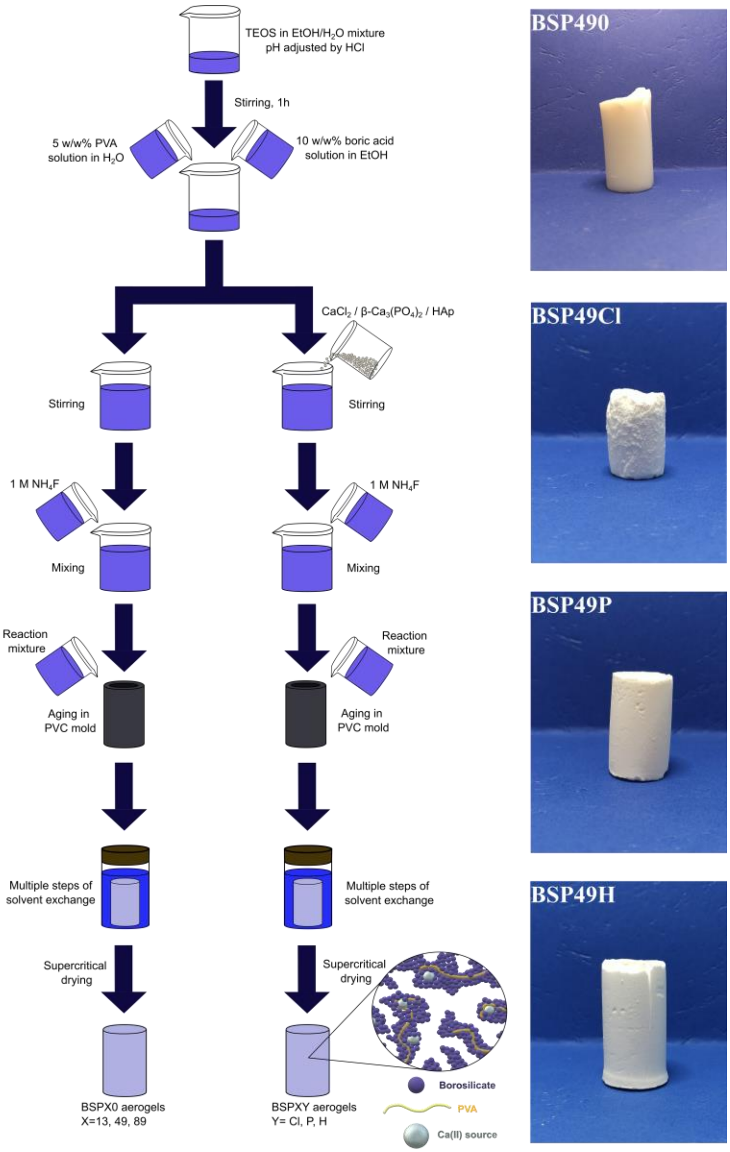

Figure 1. Synthetic scheme for the preparation of the BSPXY aerogels, and the photos of the as-prepared monolithic BSP49Y aerogels.

2. Despite the application of co-gelation, chemical bonding occurs only between PVA and boric acid due to their complex formation, while physical interactions dominate among the other components of the gel backbone. Nevertheless, these components form a homogeneous hybrid at the nanometer scale without detectable phase separation.

2.1.) The characteristic peaks corresponding to the individual components of the backbone are detected, along with the characteristic peak of the B-O-C bond, which indicates the complex formation between boric acid and PVA (**Fig. 2**). A peak would be expected around 890 cm^{-1} to indicate the presence of Si-O-B bonds, but it is not visible in any of the hybrid aerogels. FT-IR provides no information on the incorporation of $CaCl_2$; however, in the case of HAp, the presence of PO_4^{3-} is detectable. For β-$Ca_3(PO_4)_2$, the signal of PO_4^{3-} is also expected to appear, but the peak is less intense due to the smaller Ca(II)-content.

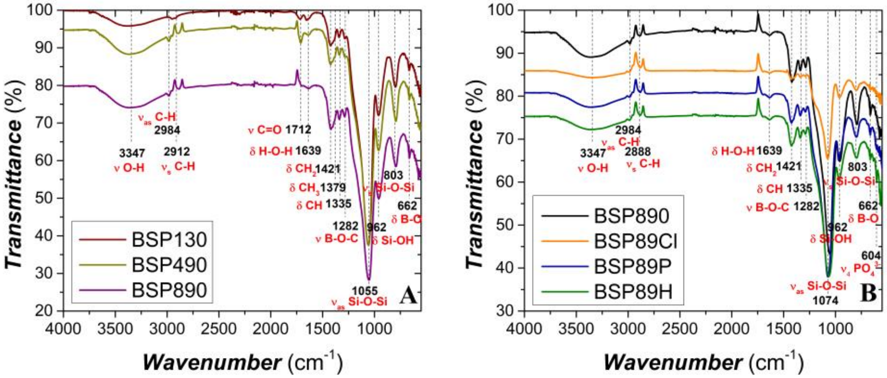

Figure 2. Infrared spectra (FT-IR) of hybrid borosilicate-PVA aerogel samples. The specific aerogels are identified in the legends. **Panel A:** The effect of different PVA sources. **Panel B:** The effect of different Ca(II) sources.

2.2.) The ^{29}Si-NMR spectra of the BSPXY aerogels show three peaks, corresponding to the Q_2 (- 91.3 ppm), Q_3 (- 100.6 ppm) and Q_4 sites (- 110 ppm), which are characteristic of $Si(OSi{\equiv})_x(OH)_{4-x}$ groups. An NMR peak would be expected at ca. 60 ppm in the spectra of the hybrid aerogels as an indication of Si-O-C bonds. In our case, this peak cannot be detected in any of the samples. The longer PVA chains result in a slight reduction of the 3D structure (Q_3+Q_4), while the incorporation of different Ca(II) sources slightly diminishes the formation of Q_4 structures (**Fig.3**).

2.3.) The ^{11}B-MAS spectra of the BSPXY aerogels show two peaks. The first signal in the range of 10-18 ppm is assigned to the trigonal BO_3 moiety, while the other one at around 0 ppm is assigned to the tetrahedral BO_4 structural element. The BO_3 peak is made up of several signals corresponding to cyclic and non-cyclic BO_3 structures. A peak around 13 ppm would indicate the presence of B-O-Si bonds. However, not even the IR spectra show a peak around 890 cm^{-1}, which could confirm the presence of such a bond. The apparent absence of these types of bonds can be explained by the fact that the formation of B-O-Si bonds is not favorable at room temperature, and they are sensitive to hydrolysis. The presence of Ca^{2+} stabilizes BO_4 units in the gel structure, promoting their increased formation. The amount of BO_4 units is highest in the BSPXH samples, as they have the greatest available surface Ca^{2+} ions due to their high Ca(II) content with relatively small particle sizes. The longer PVA chains partially cover the hydroxyapatite particles, preventing the binding of Ca^{2+} ions to the BO_4 structural units. This results in a decrease in the number of BO_4 units as the molecular weight of the PVA increases (**Fig.3**). The appearance of BO_4 groups may also result from boric acid forming complexes with PVA, reinforcing the likelihood of B–O–C bond formation.

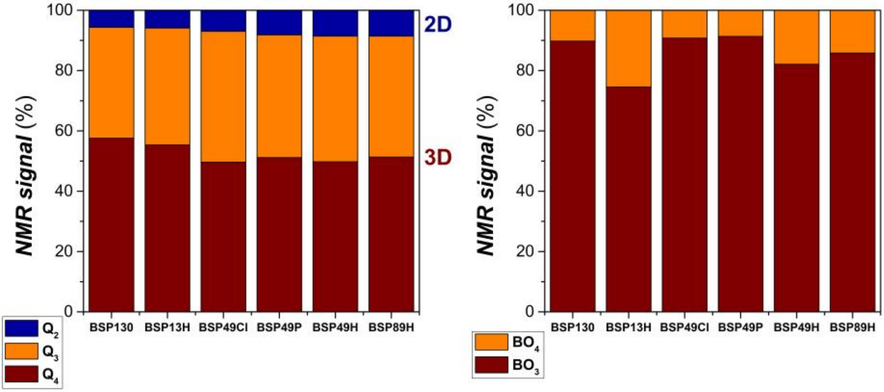

Figure 3. Left panel: 3D (Q_3 and Q_4 sites) and 2D (Q_2 site) ratio of the silica network along with the ratio of Q_2, Q_3 and Q_4 peak intensities according to ^{29}Si-MAS NMR spectra. The Q_2, Q_3 and Q_4 sites are identified in the legends. **Right panel:** The ratio of BO_3 and BO_4 intensities according to ^{11}B-MAS NMR spectra.

2.4.) The characteristic peaks of Si-OH, B-OH, C-OH, CH_2, and CH are identified in the ^{1}H-MAS NMR. In the case of BSP13Y and BSP49Y aerogels, the characteristic peak of CH_3 is also observed, due to the residual acetate group. An additional peak is observed for the BSPXH samples at 0 ppm, which is characteristic for the OH group of hydroxyapatite.

2.5.) A set of SANS experiments was performed on the BSP130 sample, filling its pore network with H_2O:D_2O mixtures with systematically changing the liquid composition. The corrected intensities were plotted as a function of the D_2O ratio at three different *Q* values, as shown in **Fig. 4.** The single minimum point around 50 (V/V)% D_2O indicates that the scattering-length density (SLD) of the mixture matches that of the aerogel backbone. Additionally the theoretical H_2O:D_2O ratio with SLD value equivalent to that of the hybrid backbone was calculated to be 51.8 (V/V)% D_2O, which is in excellent agreement with the experimental result.

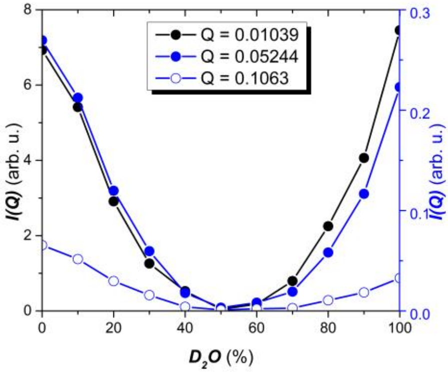

Figure 4. The background corrected scattering intensities as a function of the composition of the H_2O:D_2O mixture in the BSP130 aerogel sample plotted at three different *Q* values (*Q* = 0.01039; 0.05244 and 0.1063 Å).

2.6.) Electron microscope images prove that the network of the Ca(II)-free aerogels is consisted of an open and interconnected porous system made of primary spherical nanoparticles with a diameter of less than 10 nm (**Fig. 5.**). The pore sizes defined by the pearl-string like connection of the primary spherical nanoparticles are in the mesoporous region (<50 nm). Altering the PVA molecular weight or/and the incorporated Ca(II) source the fundamental morphological properties are retained.

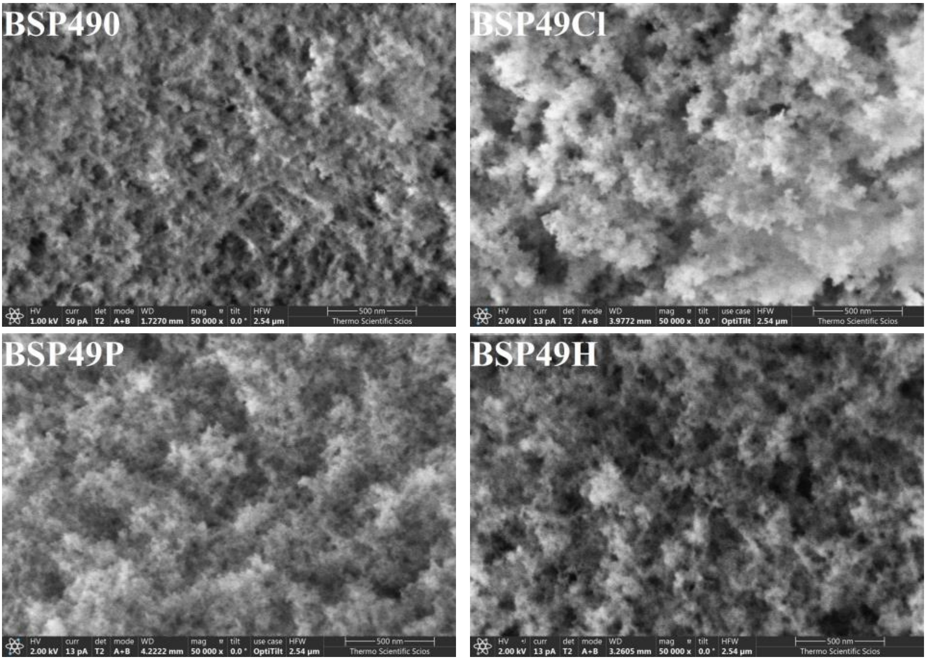

Figure 5. Low voltage scanning electron microscopy (LV-SEM) images of pristine BSP49Y aerogels in 50k × magnification**.**

2.7.) The experimental isotherms from N_2 adsorption-desorption porosimetry measurements exhibit IVa-type isotherms with H3 hysteresis loops for all samples, indicating that the BSPXY aerogels are primarily mesoporous materials, though macropores are also present. The surface area of the aerogels ranges from ca. 400 to 1040 m^2/g. Increasing the molecular weight of PVA slightly reduces both the surface area and pore volume, without significantly altering the morphology. The pore size distribution of the aerogels is altered by the incorporation of Ca(II) sources. In general, all three Ca(II) sources cause the reduction of the surface area and pore volume of the aerogels compared to the Ca(II)-free samples with the same molar weight PVA. These changes are determined by differences in the amount, particle sizes, and incorporation levels of the calcium compounds. The calculated morphological parameters are listed in **Table 1.**

Table 1. Morphological parameters of the pristine BSPXY aerogels calculated from the N_2-sorption porosimetry measurements.

Code name	**Apparent surface area (m^2/g)**	**Characteristic pore diameter (nm)**	**Pore volume (cm^3/g)**
BSP130	1038	28	6.1
BSP13Cl	763	4	2.0
BSP13P	747	22	3.7
BSP13H	579	5	3.0
BSP490	880	5	4.2
BSP49Cl	604	5	2.0
BSP49P	726	5	3.3
BSP49H	517	5	2.1
BSP890	949	26	5.0
BSP89Cl	593	4	1.8
BSP89P	665	5	2.9
BSP89H	417	5	1.7

2.8.) The SANS curves of the BSPX0 aerogels are fitted by the second level Beaucage model (**Fig. 6.**). The scattering objects of the BSPX0 aerogels at the lower structural level show an average diameter of 18-23 nm and are considered to be the pores. The scattering objects at the higher structural level display a mean size of 71-80 nm, and are assigned to the loose particle agglomerates observed in the SEM images. The power exponents vary between 2.4 and 2.9 at the lower structural level, while at the higher structural level, they range from 3.8 to 4.4. In the first case, these power exponents indicate a mass fractal structure of the pore system, while in the latter case, they provide information on the surface of the scattering object. In one experiment, the pores of the BSP130 aerogel were filled with D_2O, and in another, with a mixture containing 8 V/V% D_2O and 92 V/V% H_2O, which has a zero SLD value equivalent to that of air. The shape of the background corrected scattering curves of the wetted BSP130 aerogel is very similar to that of the dry one (**Fig. 6.**). The estimated structural parameters, along with the shapes of the scattering curves, suggest that the morphological properties of the aerogel are only slightly altered by the wetting.

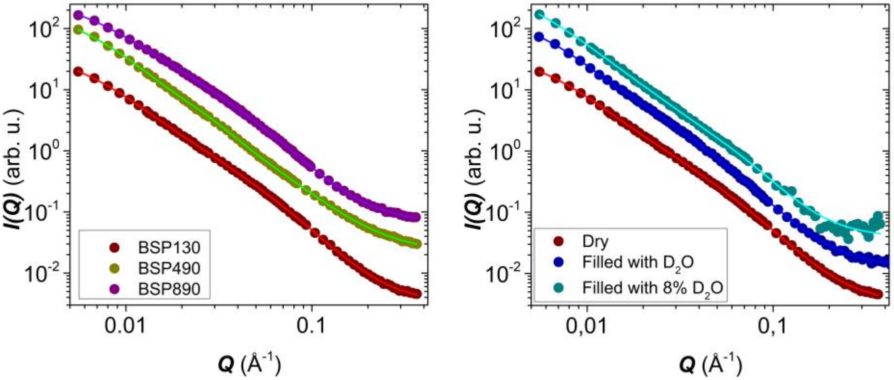

Figure 6. **Left panel:** SANS curves of the pristine BSPX0 aerogels, as given in the legend. **Right panel:** SANS scattering curves of the pristine and wetted (filled with D_2O or 8% D_2O-92% H_2O mixture) BSP130 aerogels. **Dots:** experimental data. **Lines:** results of fitting. The curves are arbitrarily shifted vertically for clarity.

3. Different Ca(II) sources were successfully incorporated into the hybrid aerogel backbone, influencing the nanostructural properties of the aerogels, but the main morphological features of the samples were remained. Suspended Ca(II)-containing aerogel microparticles attract human cells without causing any detectable toxicity.

3.1.) The presence of calcium-rich parts in the EDS elemental maps confirm the integration of the Ca(II) compounds to the aerogel backbones (**Fig. 7.**). The size of these calcium-rich parts are identical to the size of the Ca(II) sources. In BSP49Cl, the calcium-rich regions are in the nanometer range, whereas, for the other two samples, they are primarily in the micrometer range. This difference arises because $CaCl_2$ dissolves in the reaction mixture, altering its ionic strength and promoting the formation of larger aggregates. The incorporated Ca(II) likely exists in ionic form within the gel backbone, with some crystallizing as nanosized particles into the pores. Additionally, the distribution of Cl differs from that of Ca in the gel backbone. This suggests that $CaCl_2$ is incorporated in a form other than its original state. In contrast, $\beta\text{-}Ca_3(PO_4)_2$ and HAp do not dissolve in the reaction mixtures and retain their original structures upon incorporation into the gel backbone (**Fig. 7.**).

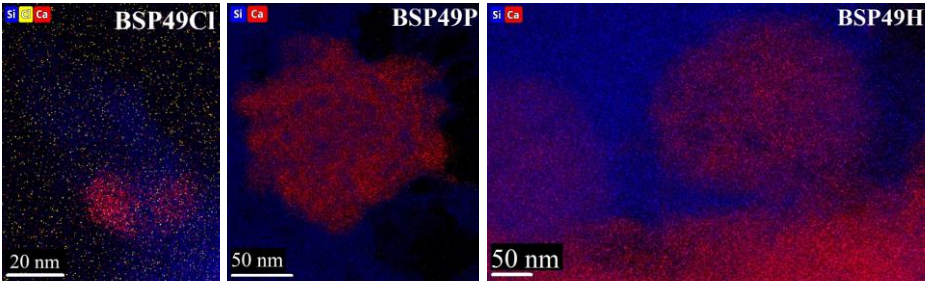

Figure 7. Elemental maps of the BSP49Y aerogels.

3.2.) Elemental analysis measurements show that the theoretically expected and measured Ca(II) contents are in good agreement for the BSP49P and BSP49H samples. However, the calcium content of the BSP49Cl sample is significantly lower than expected (**Table 2**). These results can be explained by differences in the method of incorporation.

Table 2. Ca(II) contents of BSP49Y and BSPXCl aerogels.

	BSP49Cl	**BSP49P**	**BSP49H**
Expected Ca(II) content (w/w%)	~7	~7	~10
Measured Ca(II) content (w/w)%	0.8 ± 0.1	7.5 ± 0.4	11.5 ± 0.5
Measured Ca(II) source content (w/w)%	2.1 ± 0.2	19.4 ± 0.9	28.8 ± 1.3

3.3.) The XRD spectra of BSP49P and BSP49H aerogels display characteristic peaks corresponding to the respective calcium compounds, while BSP49Cl does not exhibit XRD peaks. These prove that β-$Ca_3(PO_4)_2$ and HAp retained their original crystal structures. The absence of characteristic peaks in the spectra of BSP49Cl suggests that $CaCl_2$ was incorporated into the gel in a form other than its original crystalline state.

3.4.) The pores of the BSP13Y aerogels were filled with a 52 (V/V)% D_2O – 48 (V/V)% H_2O mixture to match the contrast of the hybrid backbone. The contrast-matched scattering curves exhibit a power-law character, except for the BSP13H aerogel (**Fig.8.**). This suggests that the scattering from either the $CaCl_2$ or the β-$Ca_3(PO_4)_2$ cannot be detected within the measured Q range. The most probable explanation is that the size of the β-$Ca_3(PO_4)_2$ particles is likely too large, and the quantity of

Ca(II) particles of BSP13Cl in the backbone is insufficient to contribute to the scattering in this way.

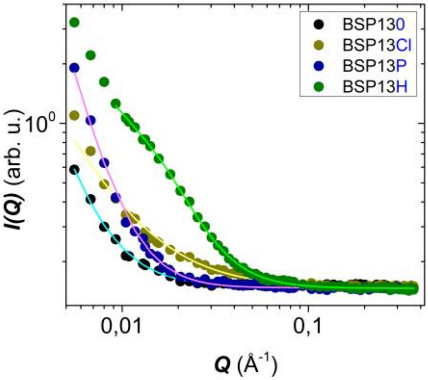

Figure 8. SANS curves of the BSP13Y aerogels filled with 52(V/V)% D_2O – 48(V/V)% H_2O mixture. **Dots:** experimental data. **Lines:** results of fitting.

3.5.) The scattering from the Ca(II) particles of BSP13Cl and the β-$Ca_3(PO_4)_2$ particles does not contribute significantly to the total scattering, thus the structural properties of these aerogels could be interpreted similarly to the case of the BSPX0 samples. However, the contribution of the incorporated calcium compounds cannot completely be neglected. The scattering from the surface of β-$Ca_3(PO_4)_2$ particles provides an additional contribution in the low Q range, making that region difficult to interpret, while the partial incorporation of the $CaCl_2$ into the hybrid backbone slightly alters the SLD of the backbone.

3.6.) The incorporation of HAp significantly alters the shape of the scattering curves of the hybrid aerogels (**Fig 9.**). The scattering curves of dry and contrast-matched BSPXH aerogels are fitted by first level Beaucage model. The scattering curves of the BSPXH aerogels are composed of contributions from pores, agglomerates, and HAp particles, which makes it difficult to assign the estimated size to one individual scattering object. However, in the case of contrast-matched scattering curves, the calculated size gives the mean size of the HAp particles that are within the SANS size range.The mean size of the incorporated HAp particles is approximately 61 nm calculated from the radius of gyration using spherical geometry, and the power exponent exhibits surface fractal characteristics.

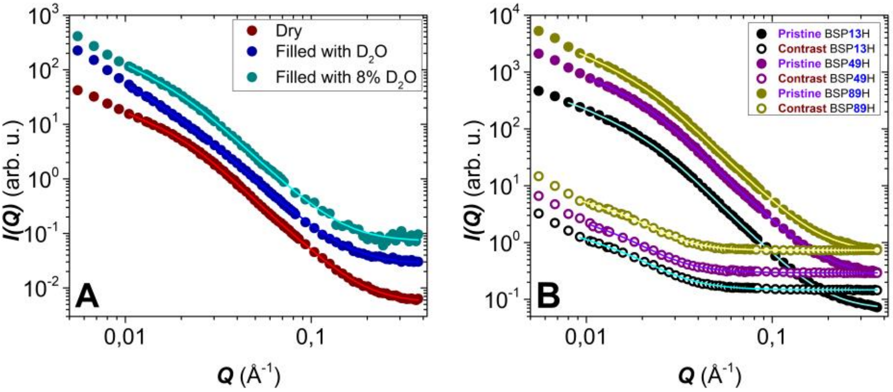

Figure 9. Panel A: SANS scattering curves of the pristine and wetted (filled with D_2O or 8% D_2O-92% H_2O mixture) BSP49H aerogels. **Panel B:** SANS scattering curves of pristine and contrast-matched BSPXH aerogels. **Dots:** experimental data. **Lines:** results of fitting. The curves are arbitrarily shifted vertically for clarity.

3.7.) To rule out the possibility of any hydration-induced morphological changes in the BSPXH aerogels, the wetting of the BSP49H aerogel was studied in details. The structural parameters of the sample remain the same when wetted with zero-SLD as in the dry state, while minor differences are observed in the case of the D_2O-wetted sample (**Fig 9.**).

Nevertheless, it can safely be concluded that the Ca(II)-doped hybrid aerogel preserves its original morphology in aqueous solutions.

3.8.) The ζ-potential of suspended BSP490 decreases from -8 to -27 mV with the increase of the pH. The incorporation of calcium compounds into the gel backbone results in higher, but still negative ζ-potentials, which can be explained by the presence of Ca^{2+} ions on the surface of the incorporated calcium compounds. These slightly negative ζ-potentials are generally favorable for cell adhesion.

3.9.) Dr. Gábor Szemán-Nagy and his team at the University of Debrecen conducted *in vitro* biological tests (monolayer regeneration of scratched cell cultures and the growth of these cultures) on BSP49Y samples that contain Ca(II) sources. DPSC (Dental Pulp Stem Cells) and MG-63 cell cultures were utilized for these biological experiments. The presence of aerogel particles attracted both types of cells, causing cells to migrate and attach directly to them. This effect initially reduced the rate of monolayer formation and the regeneration of the culture. However, by the end of the experiments (48 hours), the regeneration of the monolayer resulted in full the coverage of the particles, with homogeneous integration into the culture observed in both cases. In the case of monolayer growth assays, despite the initial delay, the generation time was comparable to that of untreated cultures by the end of the experiment. Furthermore, it was observed that increasing Ca(II) content facilitated a faster monolayer production at uniform particle concentrations

4. A structurally realistic mathematical model was developed for quantitatively analyzing small-angle scattering patterns during the progressive hydration of alginate aerogels.

4.1.) The following assumption was used to build the model: The dry aerogel has a mesoporous structure, with the solid skeleton consisting of dense polymer chains. Upon wetting, water progressively infiltrates the skeleton, potentially causing swelling and merging of swollen fibers into larger structures. Once fully saturated, these structures reach macroscopic dimensions. Throughout this process, the molecular-scale inner structure of the skeleton gradually transitions from a dry, dense polymer to a hydrogel. The scattering arising from the two-scale structure of the aerogel.

4.2.) Assuming the absence of water and polymer outside the skeleton, their local relative proportions within the skeleton are identical to the macroscopic water content of the aerogel, as

$$\varphi_w = \frac{V_w}{V_w + V_p} = \frac{\frac{V_w}{V_p}}{\frac{V_w}{V_p} + \frac{V_p}{V_p}} = \frac{V}{V+1} \qquad (1)$$

φ_w is the volume fraction of the water within the hydrated skeleton. V is the overall volume fraction of water over polymer in the macroscopic sample, and V_w (V_p) is the volume of water (polymer).

4.3.) The intensity function for the hierarchical structure is given by the Fourier transform of the scattering-length correlation function, which is expressed in a general form as

$$\bar{C}_b(r) = \langle b(x)b(x+r)\rangle - \langle b(x)\rangle^2 \qquad (2)$$

To express equation (2), the space-dependent scattering-length density $b(x)$ of the wet aerogel was determined using indicator functions $\mathrm{I}_{s/p}(\mathrm{x})$ for the skeleton and polymer contributions as

$$b(x) = \mathrm{I}_s(\mathrm{x})\left[b_w + \left(b_p - b_w\right)\mathrm{I}_p(\mathrm{x})\right] \qquad (3)$$

where b_w and b_p are the scattering-length densities of water and polymer, respectively. To distinguish between the influences of the polymer and skeleton structures on the correlation function $\bar{C_b}(r)$, their centered covariances were taken into account, assuming isotropic structures. From the practical point of view, the general intensity function $I(Q)$ is expressed as:

$$I(Q) = A \times \left\{\left[\varphi_w + \frac{b_p}{b_w - b_p}\right]^2 \frac{I_s(Q)}{\phi_s} + I_p(Q, \varphi_w)\right\} \qquad (4)$$

A is a numerical factor accounting for the measurements on a relative scale. ϕ_s is the skeleton fraction. $I_s(Q)$ and $I_p(Q, \varphi_w)$ are the Fourier transforms of the skeleton and polymer centered covariances, respectively. The initial term in the bracket addresses the scattering originating from the macroscopic structure, while the subsequent term addresses the scattering arising from the internal structure of the skeleton.

4.4.) To describe the hydration-induced structural changes of the inner structure of the skeleton, the Boolean approach was used. The centered covariance of the inner structure is expressed as

$$\bar{C_p}(r) = \left(1 - \varphi_p\right)^2\left(exp\left[\theta K_p(r)\right] - 1\right) \qquad (5)$$

where $K_p(r)$ is the geometric covariogram of the grain, which is defined as the intersection volume of two identical grains translated by a distance r relative to each other. In our case, we propose using a polymer coil as the grain. In small-angle scattering terminology, the Fourier transform of $K_p(r)$ represents the form factor of the individual polymer coils. To describe the polymer coils, the following material-specific information was used: the SLD of the alginate polymer, the volume of one individual polymer, and the radius of gyration of the polymer chain in dilute solution.

4.5.) Two approach was used to describe the scattering pattern of the skeleton. From a scattering perspective, the main characteristics of the dry aerogel are Q^{-1} scattering in the low Q range and Q^{-4} scattering in the high Q range (**Fig. 10.a**). This type of scattering is typical for fibrous structures, and to analyze it, the skeleton is modeled as a dilute suspension of elongated cylinders. However, as the characteristic size of the skeleton is beyond the measurement range above a certain water content, only the scattered intensity from its surface can be observed. In that region, it is sufficient to consider only Porod's asymptotic value of $I_s(Q)$. Notable deviations from Porod scattering are observed at low Q for water contents below 0.6 g/g (**Fig. 10.**). This indicates that at these lower water contents, the characteristic size of the skeleton is sufficiently small to scatter within the measured Q range. Within this range, only the cylinder model provides satisfactory fits.

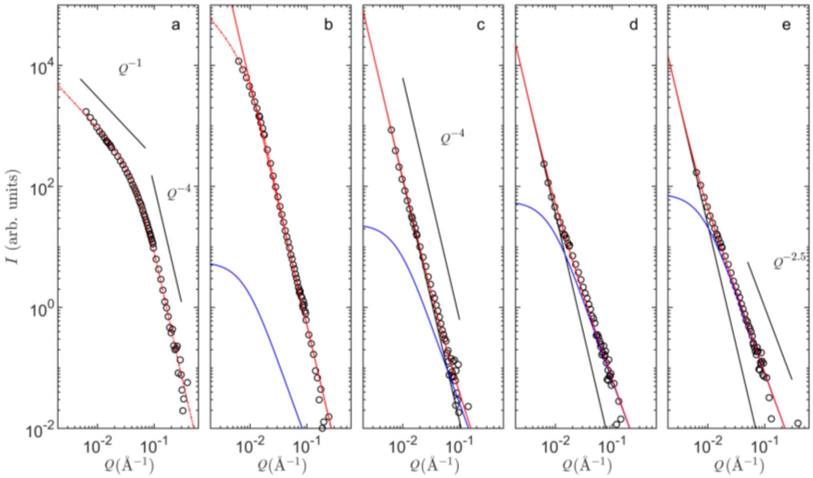

Figure 10. SANS data fits for alginate aerogel with increasing water content are as follows: (**a**) dry aerogel, (**b**) 0.33 g/g, (**c**) 0.68 g/g, (**d**) 1.1 g/g, and (**e**) 1.9 g/g. The solid lines represent the Porod model, while the dashed lines are for the cylinder model (the two models cannot be distinguished at higher water contents). The scattering contributions are displayed for the polymer solution (hydrogel) (**blue**) and the skeleton (**black**), along with their sum (**red**).

4.6.) The fitted values of median radius (R_m) indicate a two-stage wetting process. For water contents below approximately 0.6 g/g, the volume of the individual fibers grow slightly, reaching a radius of 10 nm (see inset of **Fig. 11a**). At higher water contents, the growth becomes more significant with extensive aggregation, with fiber radii extending into the micrometer range. Only this latter stage can be analyzed using the Porod model. Converting the fitted fiber parameters to an average chord length (l_s) for comparison of the two fitting approaches in the high-water-content region shows that the average chord length of the cylinders is about three times the median radius, which is in good agreement with the average chord lengths obtained from Porod model.

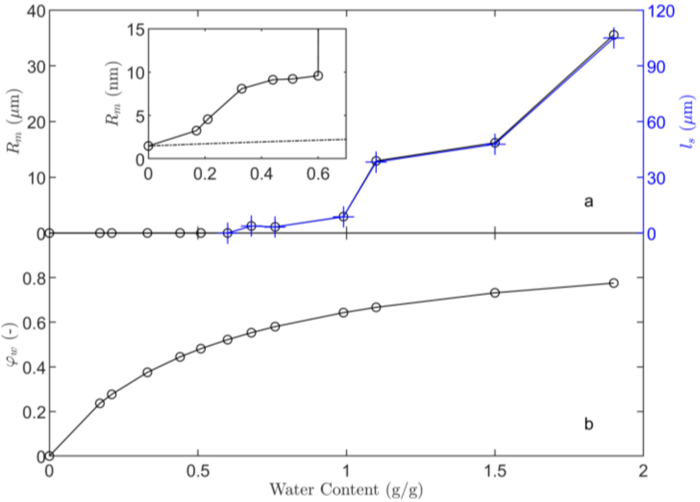

Figure 11. **Panel a:** Estimated parameters from fitting SANS patterns of alginate aerogel, shown as a function of water content: the mean skeleton chord length l_s (**blue, right axis**) and the median fiber radius R_m (**black, left axis**). The inset provides a magnified view of R_m, with the dashed line indicating the expected size due to fiber swelling alone. **Panel b:** The water fraction in the skeleton φ_w, calculated using equation (1) and applied in the fitting process.

4.7.) The SANS data analysis reveals that the wetting of alginate aerogels occurs in two distinct stages. In the first stage, with water contents below approximately 0.6 g/g, the fibers of the skeleton undergo a tenfold thickening from the dry radius R_m of 14 Å to about 100 Å. The fibrils in the dry aerogel not only swell but also aggregate into larger, yet still nanometer-sized structures. As the water content increases further, SANS reveals a dramatic structural change around 0.6 g/g, the characteristic size of the skeleton increases by more than two orders of magnitude, from nanometers to micrometers (**Fig. 11a**). This hundredfold increase in skeleton size occurs with minimal change in its water content, with the volume fraction φ_w increasing by less than 10% as the water content increases from 0.5 to 0.7 g/g. Thus, the dramatic increase in l_s results from a major rearrangement and merging of the skeleton domains, significantly reducing their total outer surface area while their volume remains nearly unchanged.The suddenness of this transition may be explained by a percolation phenomenon, where a slight increase in the size of the skeleton domains brings many into contact. Additionally, capillary forces increase with higher water content, placing the skeleton under strong compressive stress, making the nanostructure of a wet aerogel inherently unstable and prone to collapse. All these effects imminently lead to the formation of an extensive homogeneous hydrogel from the hydrated individual fibers.

IV. Possible applications of the results

Aerogels have potential applications as thermal insulators, catalyst or drug carriers, sorbents, or in tissue engineering. The field of their potential use is determined by their chemical and morphological structures.

During my doctoral research, two different types of aerogels with potential biomedical applications were investigated. The presented Ph.D. research focused on investigating the nanoscale structural characteristics of these aerogels that determine their applicability in the targeted fields.

The nanostructured hybrid aerogel microparticles show promise as suspensions for promoting bone regeneration. However, *in vivo* tests are necessary for further development. Additionally, a thorough characterization of these aerogels provides insights into the structural properties resulting from the selected synthesis route. This information can guide the design of new hybrid aerogels, allowing for the development of structures suited to specific applications.

The model we developed to analyze small-angle scattering patterns is more general than describing only the specific case of the alginate aerogel studied here. Theoretically, this model could be useful for describing the wetting of aerogels with similar chemical structures and morphological properties to alginate aerogels. In particular, it could be applied to study the wetting of other polysaccharide aerogels with fibrous nanostructures, as their molecular interactions with water and the rearrangement of their polymer tertiary and quaternary structures result in similar morphological changes. Interestingly, many structural changes observed during the wetting of aerogels are expected to occur in reverse order during the drying of solvated gels. It is hoped that the present work will be helpful in this context as well.

Publications

International publications related to the dissertation

I. Balogh, Z., Len, A., Baksa, V., Krajnc, A., Herman, P., Szemán-Nagy, G., Czigány, Zs., Fábián, I., Kalmár, J., Dudás, Z.
Nanoscale structural characteristics and in vitro bioactivity of borosilicate – polyvinyl alcohol (PVA) hybrid aerogels for bone regeneration
ACS Applied Nano Materials, 7(4), 4092-4102. (2024)
IF (2023): 5.3 (Q1)

II. Balogh, Z., Kalmár, J., Gommes, C. J.
Wetting of alginate aerogels, from mesoporous solids to hydrogels: a small-angle scattering analysis
Journal of Applied Crystallography, 57(2), 369-379. (2024)
IF (2023): 5.2 (Q1)

III. Ecsédi, B., Forgács, A., Balogh, Z., Fábián, I., Kalmár, J.
Hydration and wetting mechanism of borosilicate–Polyvinyl alcohol (PVA) hybrid aerogels of potential bioactivity
Journal of Molecular Liquids, 401, 124605. (2024)
IF (2023): 5.3 (Q1)

Other international publications

I. Herman, P., Moldován, K., Paul, G., Marchese, L., Balogh, Z., Len, A., Dudás, Z., Fábián, I., Kalmár, J.
Selective and reversible surface complexation of aqueous palladium(II) by polycarboxylate (pyromellitic acid) functionalized hybrid aerogel sorbent
Applied Surface Science, 613, 156026. (2023)
IF (2023): 6.3 (Q1)

II. Lihi, N., Balogh Z., Diószegi R., Forgács A., Moldován K., May V. N., Herman P., Fábián I., Kalmár J.
Functionalizing Aerogels with Tetraazamacrocyclic Copper(II) Complexes: Nanoenzymes with Superoxide Dismutase Activity Applied Surface Science, 611, 155622. (2023)
IF (2023): 6.3 (Q1)

III. Forgács, A., Balogh, Z., Andrási, M., Len, A., Dudás, Z., May, N. V., Herman, P., Juhász, L., Fábián, I., Lihi, N., Kalmár, J.
Mechanistic explanation for differences between catalytic activities of dissolved and aerogel immobilized Cu(II) cyclen
Applied Surface Science, 579, 152210. (2022)
IF (2022): 6.7 (Q1)

IV. Lázár, I., Forgács, A., Horváth, A., Király, G., Nagy, G., Len, A., Dudás, Z., Papp, V., Balogh, Z., Moldován, K., Juhász, L., Cserháti, Cs., Szántó, Zs., Fábián, I., Kalmár, J.
Mechanism of hydration of biocompatible silica-casein aerogels probed by NMR and SANS reveal backbone rigidity
Applied Surface Science, 531, 147232. (2020)
IF (2020): 6.707 (D1)

Hungarian conference publication

I. Balogh, Z., Lázár, I., Kalmár, J., Fábián, I., Forgács, A.
Cu(II)-ciklén tartalmú aerogél katalizátor hatásmechanizmusa
I. FKF Szimpózium: Fiatal Kémikusok Fóruma (2019)

Oral and poster presentations

Conference lecture presentations related to the dissertation

I. Balogh, Z., Kalmár, J., Gommes, C. J.
Wetting of alginate aerogels, from mesoporous solids to hydrogels: a small-angle scattering analysis
2nd International Seminar on Modelling, Simulation and Machine Learning for the Rapid Development of Porous Materials Workshop
4-6. March 2024., Madrid, Spain

II. Balogh, Z., Kalmár J., Gommes C. J.
Ca(II)-alginát aerogél nedvesedési mechanizmusának tanulmányozása kisszögű neutronszórás alkalmazásával
Hatvani István Szakkollégium 2023. Őszi Tudományos Hallgatói Konferencia
1. December 2023., Debrecen, Hungary

III. Balogh, Z., Kalmár, J., Gommes C. J.
Egy tipikus kalcium-alginát aerogél nedvesedésének mechanizmusa kisszögű neutronszórás (SANS) mérések alapján
MTA Kolloidkémiai Munkabizottság Őszi ülése
30. October 2023., Budapest, Hungary

IV. Balogh, Z., Len, A., Kalmár, J., Dudás, Z.
Funkcionalizált és hibrid aerogélek kisszögű neutronszórásos (SANS) vizsgálata
Hatvani István Szakkollégium 2022. Őszi Tudományos Hallgatói Konferencia
8. December 2022., Debrecen, Hungary

V. Balogh, Z., Baksa, V., Len, A., Szemán-Nagy, G., Moldován, K., Herman, P., Fábián, I., Kalmár, J., Dudás, Z.
Synthesis and structural investigation of borosilicate-PVA hybrid aerogels for bone regeneration application
Budapest Neutron Centre seminar
24. November 2022., Budapest, Hungary

VI. Balogh, Z., Kalmár, J., Dudás, Z.
Csontpótlásra potenciálisan alkalmas boroszilikát aerogélek előállítása és szerkezeti vizsgálata
Hatvani István Szakkollégium 2022. Tavaszi Tudományos Hallgatói Konferencia
6. May 2022., Debrecen, Hungary

VII. Balogh, Z., Veres, E., Moldován, K., Baksa, V., Szemán-Nagy, G., Fábián, I., Len, A., Dudás, Z., Kalmár, J.
Boroszilikát aerogélek mint potenciális csontpótló anyagok
II. Fiatal Kémikusok Fóruma Szimpózium
16-18. June 2021., Online

Conference poster presentation related to the dissertation

I. Balogh, Z., Dudás , Z., Kalmár, J., Len, A.
Small angle neutron scattering (SANS) investigation of functionalized and hybrid silica aerogels
Workshop on Aerogels Characterization and Modelling
29-31. March 2023., Debrecen, Hungary

UNIVERSITY of DEBRECEN

UNIVERSITY AND NATIONAL LIBRARY
UNIVERSITY OF DEBRECEN
H-4002 Egyetem tér 1, Debrecen
Phone: +3652/410-443, email: publikaciok@lib.unideb.hu

Registry number: DEENK/7/2025.PL
Subject: PhD Publication List

Candidate: Zoltán Balogh
Doctoral School: Doctoral School of Chemistry
MTMT ID: 10076745

List of publications related to the dissertation

Foreign language scientific articles in international journals (3)

1. Ecsédi, B., Forgács, A., **Balogh, Z.**, Fábián, I., Kalmár, J.: Hydration and wetting mechanism of borosilicate - Polyvinyl alcohol (PVA) hybrid aerogels of potential bioactivity.
   J. Mol. Liq. 401, 1-8, 2024. ISSN: 0167-7322.
   DOI: http://dx.doi.org/10.1016/j.molliq.2024.124605
   IF: 5.3 (2023)

2. **Balogh, Z.**, Len, A., Baksa, V., Krajnc, A., Herman, P., Szemán-Nagy, G., Czigány, Z., Fábián, I., Kalmár, J., Dudás, Z.: Nanoscale Structural Characteristics and In Vitro Bioactivity of Borosilicate-Poly(vinyl alcohol) (PVA) Hybrid Aerogels for Bone Regeneration.
   ACS Appl. Nano Mater. 7 (4), 4092-4102, 2024. ISSN: 2574-0970.
   DOI: http://dx.doi.org/10.1021/acsanm.3c05668
   IF: 5.3 (2023)

3. **Balogh, Z.**, Kalmár, J., Gommes, C. J.: Wetting of alginate aerogels, from mesoporous solids to hydrogels: a small-angle scattering analysis.
   J Appl Crystallogr. 57 (2), 1-11, 2024. ISSN: 1600-5767.
   DOI: http://dx.doi.org/10.1107/S1600576724001705
   IF: 5.2 (2023)

List of other publications

Foreign language scientific articles in international journals (4)

4. Lihi, N., **Balogh, Z.**, Diószegi, R., Forgács, A., Moldován, K., May, N. V., Herman, P., Fábián, I., Kalmár, J.: Functionalizing Aerogels with Tetraazamacrocyclic Copper(II) Complexes: Nanoenzymes with Superoxide Dismutase Activity.
   Appl. Surf. Sci. 611, 1-12, 2023. ISSN: 0169-4332.
   DOI: http://dx.doi.org/10.1016/j.apsusc.2022.155622
   IF: 6.3

5. Herman, P., Moldován, K., Paul, G., Marchese, L., **Balogh, Z.**, Len, A., Dudás, Z., Fábián, I., Kalmár, J.: Selective and reversible surface complexation of aqueous palladium(II) by polycarboxylate (pyromellitic acid) functionalized hybrid aerogel sorbent.
   Appl. Surf. Sci. 613, 1-14, 2023. ISSN: 0169-4332.
   DOI: http://dx.doi.org/10.1016/j.apsusc.2022.156026
   IF: 6.3

6. Forgács, A., **Balogh, Z.**, Andrási, M., Len, A., Dudás, Z., May, N. V., Herman, P., Juhász, L., Fábián, I., Lihi, N., Kalmár, J.: Mechanistic Explanation for Differences Between Catalytic Activities of Dissolved and Aerogel Immobilized Cu(II) Cyclen.
   Appl. Surf. Sci. 579 (30), 1-11, 2022. ISSN: 0169-4332.
   DOI: http://dx.doi.org/10.1016/j.apsusc.2021.152210
   IF: 6.7

7. Lázár, I., Forgács, A., Horváth, A., Király, G., Szemán-Nagy, G., Len, A., Dudás, Z., Papp, V., **Balogh, Z.**, Moldován, K., Juhász, L., Cserháti, C., Szántó, Z., Fábián, I., Kalmár, J.: Mechanism of hydration of biocompatible silica-casein aerogels probed by NMR and SANS reveal backbone rigidity.
   Appl. Surf. Sci. 531, 1-13, 2020. ISSN: 0169-4332.
   DOI: http://dx.doi.org/10.1016/j.apsusc.2020.147232
   IF: 6.707

Total IF of journals (all publications): 41,807
Total IF of journals (publications related to the dissertation): 15,8

The Candidate's publication data submitted to the iDEa Tudóstér have been validated by DEENK on the basis of the Journal Citation Report (Impact Factor) database.

16 January, 2025